Application of Low-Cost Transducers for Indirect In-Cylinder Pressure Measurements

# Application of low-cost transducers for indirect in-cylinder pressure measurements


## Abstract

The aim of this work is to present the results achieved in the evaluation of combustion metrics using low-cost sensors for the indirect measurement of cylinder pressure. The developed transducers are piezoelectric rings placed under the spark plugs. Tests were carried out on three different engines running in various speed and load conditions. The paper shows the characteristics of the signals generated by the piezo-ring sensors, compared to those coming from lab-grade pressure transducers: focus is to assess the achievable accuracy in the determination of frequently used combustion metrics, such as those related to knock intensity (MAPO), combustion phasing ($MFB_{10}$, $MFB_{50}$, …) and peak pressure. Despite some issues related to the variation in sensitivity (temperature effect), to mechanical noise at high engine speeds, and to signal deviation from the actual cylinder pressure trace in some portions of the engine cycle, the paper shows that combustion metrics evaluated using low-cost sensors are meaningful to be used for combustion feedback control.


## 1. Introduction

In recent years, regulations have imposed tighter limits for pollutant emission, which are hazardous for human health [1, 2, 3]. Furthermore, the introduction of Real Driving Emission (RDE) tests challenged vehicles performance, forcing automotive makers to demonstrate emissions compliance over a variety of boundary conditions such as temperature, altitude, and driving style [4]. Stricter regulations, along with the need to reduce fuel consumption (hence CO2 emissions [5, 6]), pushed automotive manufacturers to investigate new internal combustion engines technologies. In fact, the objective of these regulations for light duty vehicles homologation is to push automotive manufacturers and Original Equipment Manufacturers (OEMs) towards greener technologies (vehicle electrification [7, 8], hydrogen [9], alternative fuels [10]) in order to lower the environmental footprint and, in the end, move towards a carbon neutral society.

Vehicle electrification is seen as perhaps the most promising option in order to drastically lower fossil fuel consumption [11, 12]: however, as found in other research [13, 14] this should not be the only solution for the reduction of $CO_2$ emissions. Furthermore, electric powertrains are still facing challenges related to:

- short operating range
- long recharging time
- limited recharging station infrastructure

All these issues can be solved, [15] but switching from traditional vehicles (gasoline, diesel) to completely electric powertrains requires time. For this reason, change is expected to be progressive, starting from the development and spreading of hybrid [16, 17, 18, 19] vehicles as already seen today. This means that combustion engines should still be present for at least the next 15 years [20].

In this scenario, in recent years research on Internal Combustion Engines (ICEs) has focused on “innovative combustion techniques” [21, 22, 23]. This term includes different types of combustion (Gasoline Direct Compression Ignition (GDCI) [24], Reactivity Controlled Compressed Ignition (RCCI) [25], Spark Assisted Compressed Ignition SACI [26], Turbulent Jet Ignition (TJI) [27, 28]) which leverage different heat release mechanisms, with respect to the traditional compression- and spark-ignition processes. The most interesting characteristic of innovative combustion techniques is the capability of achieving higher efficiency and lower pollutant emissions.

Another solution that is being proposed for the energy transition toward a carbon neutral society is the development of synthetic fuels (methane [29, 30], hydrogen [31, 32], synthetic gasoline [33, 34]) to be used

instead of fossil fuels. The advantage of such fuels would be the possibility of capturing $CO_2$ from the atmosphere or industrial processes during the production phase [29, 30 , 31, 32] and the possibility of storing large amounts of energy during peaks of production of renewable energy plants. In fact, part of the surplus-energy generated during production peaks cannot be efficiently stored in batteries. in addition, synthetic fuels are characterized by high energy density (especially when compared to batteries), making them perfect energy carriers.

Hydrogen is one of the most promising candidate energy carriers for the energy transition from fossil fuels [35, 36]. One of the possible hydrogen applications is its use as fuel for ICEs. Hydrogen, in fact, is compatible with traditional spark ignited engines with relative minor modifications [37, 38]. Both hydrogen and innovative combustion techniques may exhibit more impulsive or unstable heat release, requiring feedback control of the process: the sensitivity to factors like intake air temperature is such that a feed forward approach would result in undesired effects [39]. Hydrogen combustion for example is extremely prone to knocking phenomena in stoichiometric conditions [40, 41]. In order to bring the abovementioned technologies (Low Temperature Combustions, hydrogen, etc.) on production cars, control of the combustion process based on cylinder pressure information is vital [42, 43]. The major issue with this approach is chosen-sensors costs: for this reason, in recent years, much research has been focused on the development of methodologies for extracting useful combustion information from low-cost sensors.

Accelerometers installed on the engine block, generally used to evaluate the knock intensity, may also allow to determine the maximum pressure angle, $MFB_{50}$ and diagnose misfire, then an appropriate "closed-loop" control with such tools is possible [42]. However, due to unwanted mechanical noise the accuracy tends to fall at high engine speed. Crank speed fluctuations detected by means of Hall effect or variable reluctance sensors are used for misfire detection in on-board application, however it is also possible to determine indicated torque and the $MFB_{50}$: once again, the estimation of the combustion metrics with such methods is very sensitive to speed and load [44, 45]. Other approaches are based on the analysis of engine acoustic emissions, but the need to isolate the useful content of the signal from the background noise, leads to interesting results only in the domain of high frequencies [44, 46]. Detection of the force on cylinder head components is another method to estimate the pressure inside the combustion chamber [47]. The most common measurement devices position is under the spark-plug, in this way the force seen by the sensing element is linearly related to the pressure inside the cylinder. However, these systems usually require the processing of the engine head or the modification of the standard components present inside the engine [48, 49, 50]. Other configurations have been studied over the years [51].

The differences between the proposed sensor and other similar applications mainly consist in a very simple design, making the assembling easier. The quartz machining allows small thickness, which is crucial to reduce axial footprint. In [52], the authors showed the first results concerning the development of a low-cost sensor in which the sensing element was a piezo electric ring placed beneath the spark replacing the series washer. Here, the first part of the paper presents the design of a new prototype. The second part focuses on the analysis of results obtained using these new prototypes on three different engines: performance is assessed by comparing some of the most used combustion metrics evaluated via low-cost prototypes with those obtained with lab-grade transducers. The following metrics will be considered:

- Combustion Angles ($MFB_{10}$, $MFB_{50}$).
- MAPO (Maximum Amplitude of Pressure Oscillations) knock intensity index
- Peak pressure and Angle of Peak pressure.

These metrics were selected due to their more relevant applicability for closed loop controls. $MFB_{90}$ and IMEP were missing because were more difficult to be estimated [52].

## 2. Sensor Description

The sensing parts of the sensor consist of a ceramic piezoelectric ring contained between two sheets of Printed Circuit Boards (PCB) where the contacts for the signal cable are located. The cable is a single coaxial cable with 1 mm diameter so as to avoid issues related to electrical noise. The necessary mechanical sturdiness has been achieved by encapsulating the sensor stack in a metal case which keeps all sensing components tied together, thus limiting the potential damages to the quartz parts during mounting and dismounting operations. The case keeps inside the sensing elements thanks to an interlocking mounting and the use of epoxy resin placed inside during the assembly operation. (Figure 1) The epoxy resin not only acts as an adhesive, but also as an electrical insulator (electrical resistance greater than $10^{15}$ Ohm-cm) greatly improving the signal to noise ratio.

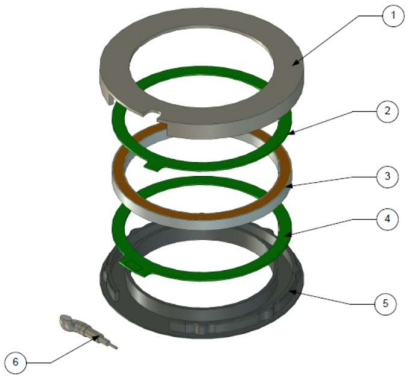


**Figure 1. Example of Piezo-electric upgraded prototype. 1 upper case, 2 positive contact, 3 piezo-electric ring, 4 negative contact, 5 lower case, 6 signal wire.**

Two versions of this prototype washer sensor were developed, compatible with M10 and M12 spark plugs. The two versions were tested on three different gasoline engines, whose characteristics are reported in Table 1. A total of 312 tests were carried out on eddy current dynamometers manufactured by Borghi&Saveri, running the engines in various operating conditions, with the aim of assessing the sensor capability of estimating cylinder pressure, allowing the accurate evaluation of combustion metrics.

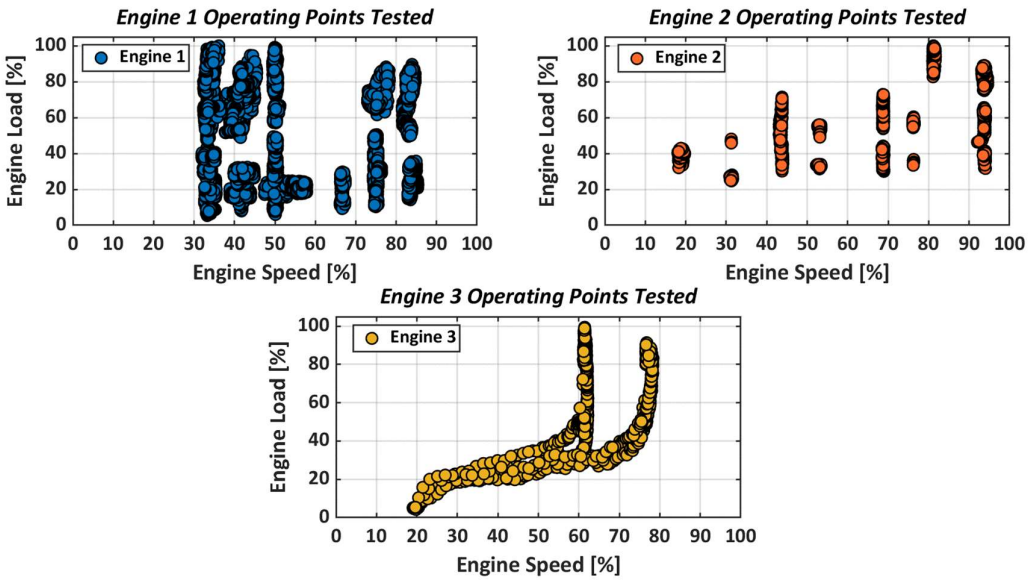


**Figure 2. Engine operating points tested on the test bench for the different engines.**

Table 1. Characteristics of the engines tested using piezo-electric washer sensors.

| | Engine 1 | Engine 2 | Engine 3 |
|---|---|---|---|
| Manufacturer | Fiat Chrysler Automobiles | Ferrari | Fiat Chrysler Automobiles |
| Strokes for Cycle | 4 | 4 | 4 |
| Geometry | In-line, 4 cylinder | V, 8 cylinder | In-line, 4 cylinder |
| Type | Gasoline GDI, Supercharged | Gasoline GDI, Turbocharged | Gasoline PFI, Supercharged |
| Displacement (cm3) | 1995 | 3990 | 1368 |
| Stroke (mm) | 84 | 88 | 72 |
| Bore (mm) | 90 | 82 | 84 |
| Compression Ratio | 10:1 | 9.5:1 | 9:1 |
| Equipped Spark Plug | M12 | M10 | M12 |
| # Cylinders Equipped with Piezo-Electric Washer Sensors | 1 | 3 | 1 |

All engines were equipped with one or more piezo-electric washers, and cylinders equipped with washers were also fitted with a high-precision pressure sensor, used as reference. For engines 1 and 3, the reference sensor was integrated in a measuring spark plug, while for engine 2 standard M5 pressure transducers were installed on a modified cylinder head. Figure 2 shows the operating conditions for the assessment of sensor performance, on all engines. It must be highlighted that the engine load was normalized with respect to the maximum IMEP value measured during the engine testing, while engine speed was normalized with respect to the maximum allowed for each engine shown in Table 1.

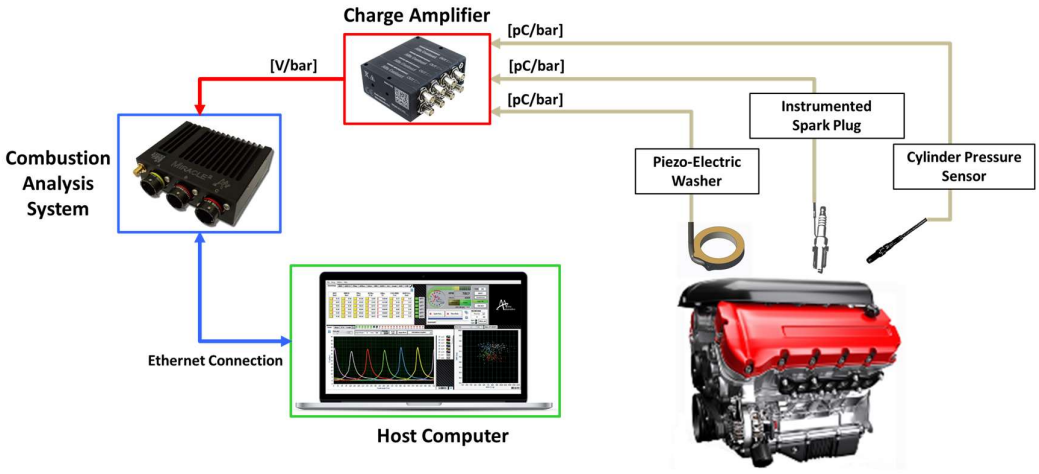


Figure 3. Schematic of the toolchain used for the acquisition of all the cylinder pressure sensors.

Figure 3 reports a sketch of the toolchain used to acquire signals: a charge amplifier is used both for reference and prototype sensors. Amplifiers add cost, which should be taken into consideration for cost-sensitive applications: future tests will be dedicated to tackling this issue, by either developing a low-cost charge amplifier, or by assessing quality of combustion metrics evaluated without the use of this component.

The following sections present and discuss on-engine results.

## 3. Prototype Sensor Signal

The present section focuses on the description of the washer signal characteristics.

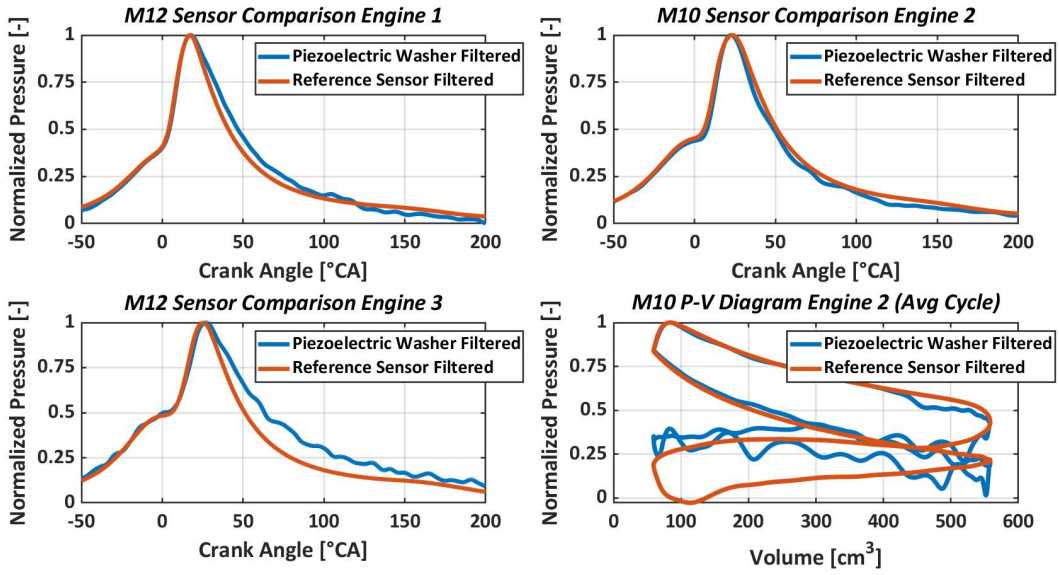


**Figure 4. Comparison between the reference sensor and the piezo-electric washer sensor for the three engines. The curves are normalized with respect to the maximum pressure peak measured with the respective sensor, so that the maximum values for both sensors is coincident. Engine 1, single cycle at operating point: Engine Speed = 74.5 % @ Engine Load = 47.5 % @ relative MFB50 = 0.1 °CA; Engine 2 (cylinder 6), single cycle at operating point: Engine Speed = 81.25 % @ Engine Load = 90.9 % @ relative MFB50 = 4.21 °CA; Engine 3, single cycle at operating point: Engine Speed = 61.55 % @ Engine Load = 40.9 % @ relative MFB50 = 4.6 °CA. Engine 2 (cylinder 6) P-V diagram referring to average traces of 100 cycles (pressure in logarithmic scale) : Engine Speed average = 81.25 % @ Engine Load average = 90 % @ relative MFB50 average = 6 °CA .**

Figure 4 presents the comparison between washer and reference sensor signals over a portion of an engine cycle, for the three engines. The figure clearly shows that the piezo-electric washer is affected by a pressure misestimation during the expansion stroke. This issue was already reported in [52], where an overestimation of the cylinder pressure during the expansion stroke was observed. The data collected show that the misestimation depends on the running condition, and the engine under test: while in engine 1 and 3 (M12 washer) pressure is overestimated, in engine 2 (M10 washer) it is underestimated.

The reason of this deviation may reasonably attributed to thermal effects [53]. This issue is critical, since it greatly affects the evaluation of IMEP and Rate Of Heat Release (ROHR), and the corresponding combustion metrics ($MFB_{10}$ and $MFB_{50}$ ) as previously verified in [52].

Another issue affecting prototype sensor is variation of sensitivity, both in terms of part-to-part dispersion and change with temperature. Figure 5 shows the normalized pressure traces obtained on three cylinders for the same cycle. The normalization was carried out with respect to the maximum measured by the reference sensor of cylinder 7. Comparing washer and reference sensor signals: it is clear that the three prototypes have different sensitivities, while the maximum pressure peak detected by the reference sensors is similar, that measured with the prototypes varies considerably from part to part.

Such dispersion can be partly explained by considering the prototypes manufacturing process which is not optimized yet. The epoxy resin used to connect all the prototype parts is added by hand inside the sensors,

hence the quantity of resin that eventually remains inside the sensor could be different from sensor to sensor, leading to a variation in stiffness, henceforth sensor sensitivity.

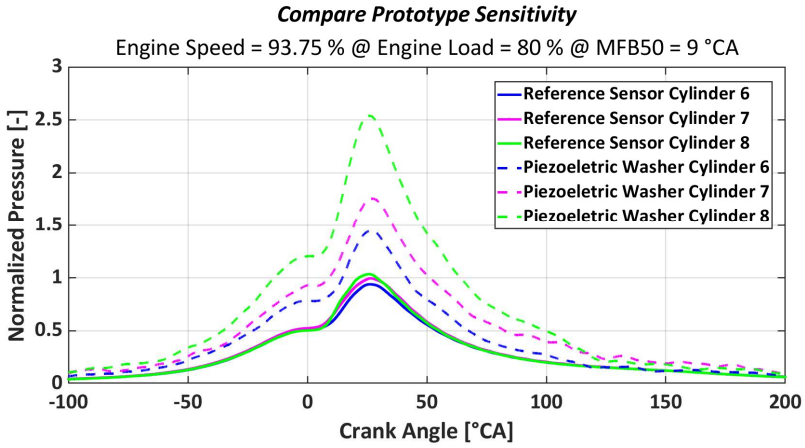


**Figure 5. Example of sensor linearization disparity on engine 2.**

Furthermore, stiffness is sensitive to engine temperature: in Figure 6, ratio between peak pressure evaluated with reference sensor and piezoelectric washer is reported against engine coolant temperature. Figure 6 also shows that variations with temperature are far lower if the spark plug is tightened with a higher torque.

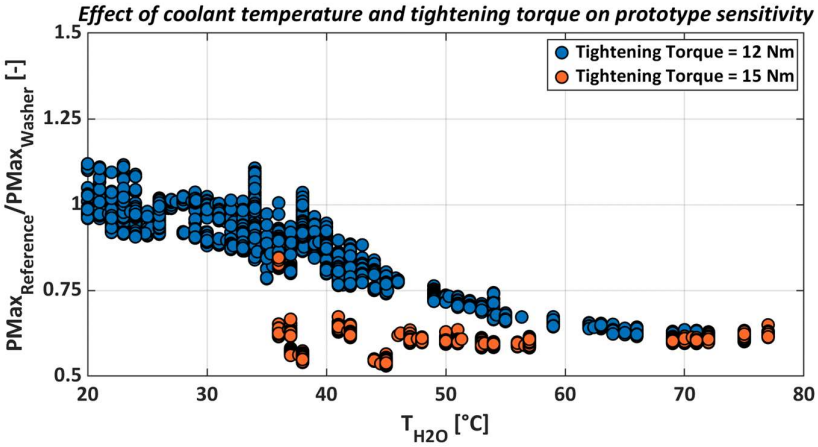


**Figure 6. Effect of coolant temperature and tightening torque on prototype sensitivity. Tests performed on engine 1 run in idle.**

The impact of stiffness on sensor sensitivity can be explained by analysing the stresses acting on the component with running engine. The piezoelectric washer is capable of measuring the pressure inside the cylinder thanks to the interaction of two forces that are transferred from the threaded connection of the spark plug to the piezo-electric washer. The first one is the tightening force generated during the mounting operation of the spark plug. Slowly varying forces should be compensated by pegging and/or amplifier drift compensation. Unless they change the sensitivity as may be the case here. The second force varies according to the pressure inside the cylinder. The two forces have always opposed directions, since the action of the gases against the spark plug tends to loosen the preload. Hence, the piezo-electric washer is sensitive to the reduction of tightening force resulting from the action exerted by combustion pressure on the spark plug.

This interaction of forces can be described by the bolted joint diagram represented in figure 23.13 in [54]. The diagram shows on the y axis forces exerted on the threaded junction, while the corresponding strains of bolt (spark plug) and joint (piezo-electric washer) are reported on the x-axes. At the end of the mounting

process, on both bolt and joint a preload force ($F_p$) is exerted, stretching the spark plug and squeezing the piezo-electric washer. The strains of the two elements are:

$$\Delta L_b = \frac{F_p}{E_b} \ (Eq.1)$$

$$\Delta t_j = \frac{F_j}{E_j} \ (Eq.2)$$

Where $\Delta L_b$ and $\Delta t_j$ are bolt and joint deformation, $F_p$ is preload force, $E_b$ and $E_J$ are Young moduli of bolt and joint, respectively. Figure 23.13 in [54] represents a situation in which an additional force is applied to the bolt. In this case, the additional force is divided between the two elements and while the force applied to the bolt increases, the joint is unloaded. So, the additional force is equal to the sum of forces that are applied to bolt ($\Delta F_b$) and joint ($\Delta F_c$):

$$F_x = \Delta F_c + \Delta F_b \ (Eq.3)$$

Since strain variation ($\Delta\delta$) is equal for the two elements it is possible to express the deformation as a function of the additional load:

$$F_x = E_j * \Delta\delta + E_b * \Delta\delta \ \rightarrow \ \Delta\delta = \frac{\mathrm{F_x}}{E_j + E_b} \ (Eq.4)$$

The resulting tensile force acting on the spark plug is thus obtained by summing preload force and external force:

$$F_b = \Delta F_b + F_p \ \rightarrow \ F_b = F_p + F_x * \frac{E_b}{E_b + E_j} \ (Eq.5)$$

The force on the joint (piezo-electric washer) can finally be determined as:

$$F_j = \Delta F_c - F_p \ \rightarrow \ F_j = F_x * \frac{E_j}{E_b + E_j} - F_p \ (Eq.6)$$

Equation 6 allows to appreciate how forces conveyed through the threaded connection are heavily influenced by the Young modulus of spark plug thread and piezo-electric washer. Young modulus is not independent of material temperature [55, 56, 57, 58]. This is true for both washer, especially due to the presence of resin, and thread, due to the intense heat flux and extreme temperatures: thread and sensor stiffnesses may vary significantly. As Equation 6 states, changes in materials stiffness affect forces stressing the sensor as a result of a given external force, i.e., the amplitude of the signal generated by the quartz for a given cylinder pressure, which implies a change in sensitivity.

As next sections will show, the sensor allows to accurately evaluate combustion metrics, regardless of the issues listed above.

## 4. Combustion Phasing Estimation

The first group of combustion metrics that was investigated can be referred to as “combustion angles”: $MFB_{10}$, $MFB_{50}$, and Firing $AP_{max}$ were taken into consideration.

MFB metrics indicate the crank angle positions where a given fraction of the fuel introduced in the combustion chamber is burnt. Most frequently used combustion angles are:

- $MFB_{10}$: related to the start of combustion; it can be used to detect autoignition phenomena [59, 60].

- $MFB_{50}$: centre position of the energy release; crucial to optimize the combustion process, since it synthesizes the effect of the reactions ignition and propagation. Best engine efficiency is reached for a narrow range of $MFB_{50}$, thus it is frequently used as a target for closed loop control approaches. [42, 43]
- The third combustion angle is the Firing $AP_{max}$ which is defined as the crank angle position where the maximum pressure is reached, within an angular window where the combustion takes place.

### *4.1.1 $MFB_{10}$ and $MFB_{50}$ Estimation*

The present section illustrates the results obtained in the determination of $MFB_{10}$ and $MFB_{50}$ for the three engines used during the tests. Combustion angles were evaluated using the same approach for the washer and the reference sensors.

For both signals the ROHR is calculated via the well-known equation [61]:

$$ROHR = \frac{k}{k-1} * P(\theta) * \frac{dV(\theta)}{d\theta} + \frac{1}{k-1} * V(\theta) * \frac{dP(\theta)}{d\theta} \ (Eq.7)$$

Then, starting from the ROHR the Cumulated Heat Release (CHR) is evaluated as the integral of ROHR within an angular window containing the whole combustion process.

$$CHR = \int_{\vartheta_{start}}^{\vartheta_{end}} ROHR(\theta) * d\theta \ (Eq.8)$$

k is considered constant and equal to 1.3 for both ROHR and CHR. $CHR_{max}$ is calculated as the difference between maximum and minimum values assumed by CHR within the combustion window. Combustion angles are determined as the crank angle position where CHR curve reaches a given percentage of maximum heat release (10% for $MFB_{10}$, and 50% for $MFB_{50}$).

Evaluation of CHR is carried out by using different windows for the reference sensors and the piezo-electric washers. For all reference sensors, starting position of the angular window ($\theta_{start}$) is set to 30° BTDC while the end ($\theta_{end}$) is placed at 110° ATDC. On the other hand, for all the prototypes (both M12 and M10), while $\theta_{start}$ angle is kept at 30° BTDC, $\theta_{end}$ angle is set 20 degrees after ROHR peak. This helped tackling the issues related to misestimation of cylinder pressure during expansion, which could impact the evaluation of maximum value of CHR ($CHR_{max}$), hence in determining $MFB_{10}$ and $MFB_{50}$.

The evaluation of ROHR according to Eq. 7 is performed after processing the signal to recover the actual average value: in fact, as both washer and reference sensor use a charge amplifier, signals are high-pass filtered, thus they require cycle-by-cycle pegging [62, 63, 64]. Although the heat release curve shape is indifferent of the sensor sensitivity/gain (Volt/bar characteristic), it is affected by the signal average value: in fact, while the two terms on the right side of Eq. 7 are equally affected by the gain of the pressure signal, adding an offset would only affect the first term. This means that sensor sensitivity and amplifier gain affect ROHR as scaling factors, preserving the shape, but the signal offset changes the ROHR trace shape. Changes in ROHR (and consequently, CHR) shape may impact $MFB_{10}$ and $MFB_{50}$ evaluations.

Since Manifold Air Pressure (MAP) sensor data were not available for all tested configurations, the polytropic method [62, 63, 64] is used for the reference sensor signals, and estimated MAP is then used also for washer signals.

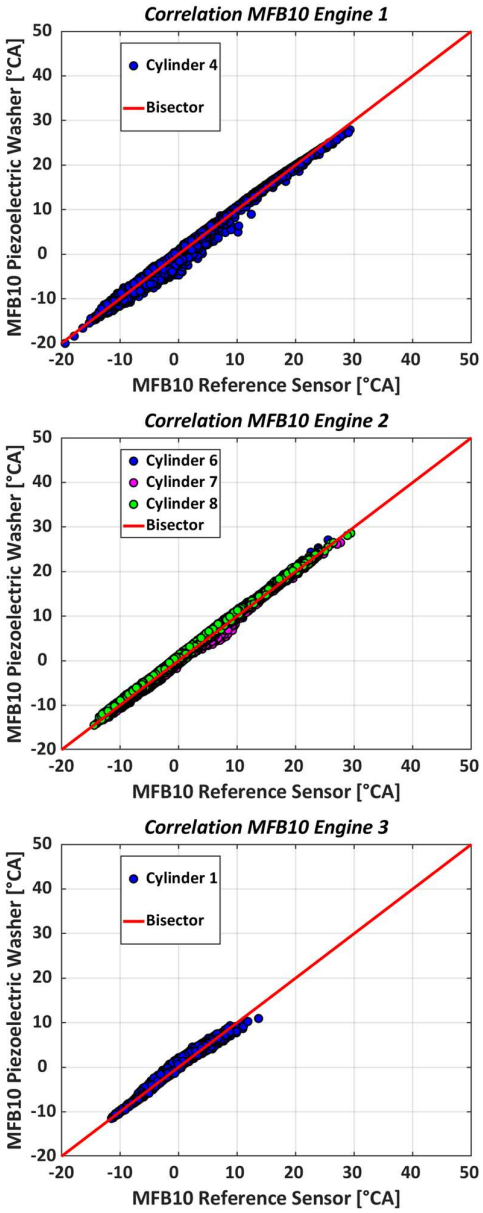


**Figure 7. MFB10 correlation results. All operating points, all engine cycles. MFB10 offset equal to average calculated from reference sensor.**

Figure 7 compares $MFB_{10}$ values evaluated using the washer with those obtained using reference sensors. The three plots refer to the three engines: all available engine cycles, pertaining to various running conditions, are reported in the figure. All combustion metrics are offset, by subtracting the average $MFB_{50}$ value. The correlation of the two metrics is very strong, and the standard deviation is small.

Root Mean Square Error (RMSE) and R squared ($R^2$) referring to all tests are reported in Table 2: for all prototypes, RMSE is lower than 0.6° CA. Results consistency achieved with different prototypes on three different engines gives confidence of the robustness of the washer sensor for the estimation of $MFB_{10}$.

**Table 2. Washer-derived MFB10 estimation quality for the different engines: correlation with reference sensors for all tested operating points.**

| $MFB_{10}$ | | | |
|---|---|---|---|
| # Engine | Instrumented Cylinder | RMSE [°CA] | $R^2$[-] |
| 1 | Cylinder 4 | 0.53 [°CA] | 0.9971 [-] |
| 2 | Cylinder 6 | 0.49 [°CA] | 0.9985 [-] |
| | Cylinder 7 | 0.48 [°CA] | 0.9979 [-] |
| | Cylinder 8 | 0.58 [°CA] | 0.9984 [-] |
| 3 | Cylinder 1 | 0.50 [°CA] | 0.9945 [-] |

Coming to the evaluation of $MFB_{50}$, errors obtained using the prototypes signal are slightly higher compared to those regarding $MFB_{10}$. However, as Table 2 shows, correlation is still very high and RMSE is always lower than 1 °CA which confirms the usability of washers for combustion phasing feedback control.

**Table 3. Washer-derived MFB50 estimation quality for the different engines: correlation with reference sensors for all tested operating points.**

| $MFB_{50}$ | | | |
|---|---|---|---|
| # Engine | Instrumented Cylinder | RMSE [°CA] | $R^2$[-] |
| 1 | Cylinder 4 | 0.86 [°CA] | 0.9987 [-] |
| 2 | Cylinder 6 | 0.96 [°CA] | 0.9983 [-] |
| | Cylinder 7 | 0.55 [°CA] | 0.9982 [-] |
| | Cylinder 8 | 0.52 [°CA] | 0.9984 [-] |
| 3 | Cylinder 1 | 0.32 [°CA] | 0.9993 [-] |

What is interesting to notice is that for engine 1 and the first cylinder of engine 2, $MFB_{50}$ evaluation presents a higher-than-average RMSE, with respect to results for $MFB_{10}$ (from 0.5 °CA to 0.8 °CA), while for engine 3 the effect is opposite.

These differences are related to mechanical noise: in fact, for the first and second engine the noise affecting the signal was centred on the expansion stroke, leading to a greater impact on the estimation of the $MFB_{50}$. On the contrary, for the third engine the noise was higher at the end of the compression stoke thus worsening the estimation of the $MFB_{10}$. In the case of the third engine, after the test it turned out that the signal cable was pinched during mounting, and consequently electric insulation was defective: electric noise produced by coil discharge worsened the evaluation of $MFB_{10}$.

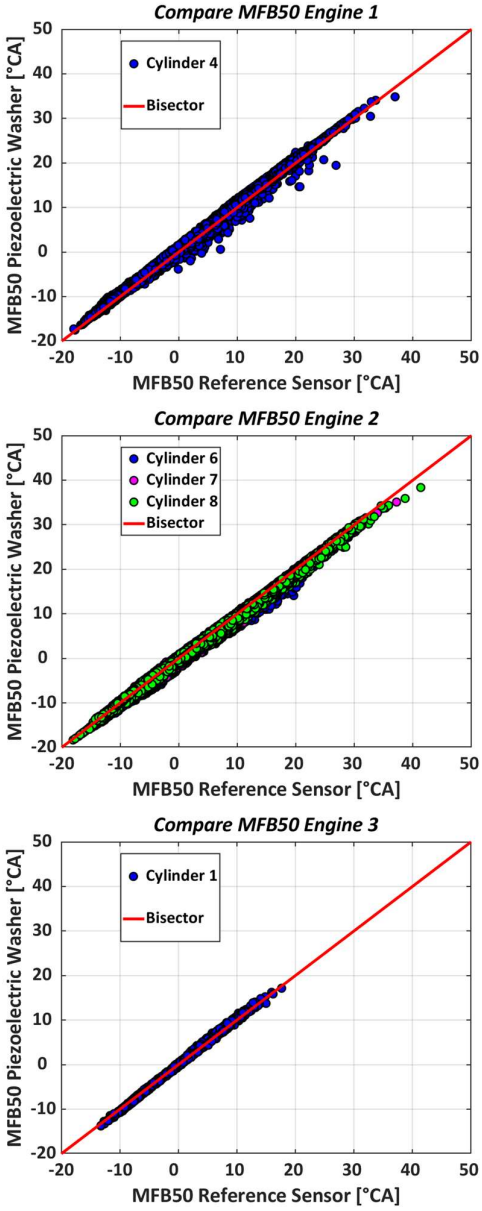


**Figure 8. MFB50 correlation results. All operating points, all engine cycles. MFB50 offset equal to average calculated from reference sensor.**

Despite the effects related to undesired mechanical and electrical noise, Figure 8 allows to appreciate that a good evaluation of $MFB_{50}$ can be achieved for all three engines.

### *4.1.2 Firing $AP_{max}$ Estimation*

This section presents results regarding evaluation of Firing $AP_{max}$ angle. This angle is different from the peak pressure location: in fact, in case of delayed combustions (for example in idling, or in catalyst heating), pressure peak is reached at the end of compression stroke, so it does not carry information on combustion process.

To overcome this issue, in the present work peak pressure is only searched for over the portion of the pressure bell where the combustion takes place (according to Equation 9 below), and firing $AP_{max}$ is determined accordingly.

$$Firing\ P_{MAX} = Relative\ Max(Cylinder\ Pressure]_{SOC}^{EOC})\ \ (Eq.9)$$

For convenience, $MFB_{10}$ is considered as the window start for Firing $AP_{max}$ search, and a fixed window duration of 100° is used for all engine cycles within the dataset.

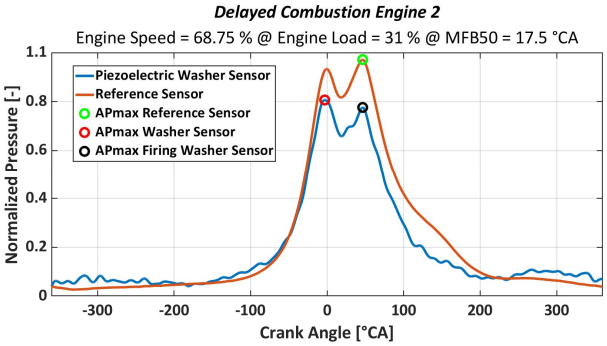


**Figure 9. Calculation of Firing APmax and 'standard' APmax . Pressure traces were normalized with respect to the maximum pressure peak measured with the reference sensor. Data from cylinder 6 engine 2, single engine cycle.**

Figure 9 shows that $AP_{max}$ and Firing $AP_{max}$ may be superimposed (reference sensor) or may be significantly different (washer sensor): in the engine cycle reported in the figure, the error in determining $AP_{max}$ would be significant, even if the shape of the pressure bell detected with the two sensors is similar. This may lead to apparently large errors in the estimation of peak pressure location. The use of Firing $AP_{max}$ solves this problem.

**Table 4. Washer-derived Firing APmax estimation quality for the different engines: correlation with reference sensors for all tested operating points.**

| Firing $AP_{max}$ | | | |
|---|---|---|---|
| **# Engine** | **Instrumented Cylinder** | **RMSE [°CA]** | **$R^2$[-]** |
| **1** | **Cylinder 4** | **0.59 [°CA]** | **0.9980 [-]** |
| **2** | **Cylinder 6** | **0.69 [°CA]** | **0.9979 [-]** |
| | **Cylinder 7** | **0.67 [°CA]** | **0.9959 [-]** |
| | **Cylinder 8** | **0.62 [°CA]** | **0.9965 [-]** |
| **3** | **Cylinder 1** | **0.57 [°CA]** | **0.9964 [-]** |

Table 4 collects RMSE and $R^2$ relating the firing $AP_{max}$ indices evaluated using prototype sensors to those determined with reference sensors. Once again, the strong correlation between the two sensors outputs is confirmed: for all datasets RMSE is lower than 0.7 °CA, thus the estimation of this index is accurate enough for on-board applications.

Results presented in Sections 3 and 4 considered all available data. Sections 5 and 6 will only focus on data sampled on engine 2, where heavy knocking cycles were acquired, allowing a significant comparison of knock intensity indices calculated with the two sensors, on three different cylinders. The same dataset will be used to compare evaluation of maximum pressure ($P_{max}$): this choice is related to the availability of ECU data which are used for the determination of $P_{max}$ using the washer signal.

## 5. MAPO Estimation

This section presents the analysis carried out to assess washer sensor capability to detect knock intensity, over a variety of working points. Figure 10 summarizes explored running conditions in terms of engine speed, load, and $MFB_{50}$ range values.

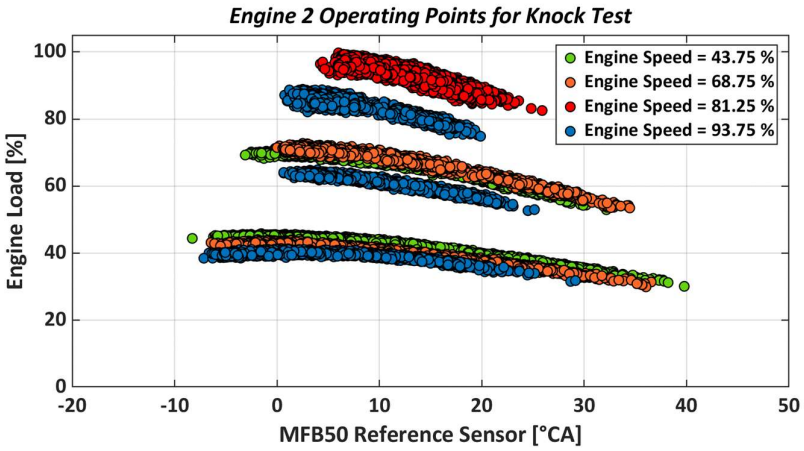


**Figure 10. Operating points and MFB50 sweep tested for the knock study on engine 2.**

The use of piezoelectric load washers under the spark plug as knock measurement has already been considered in the past [52, 65]. However in this paper, knock intensity is estimated with a different approach compared to previous work on this subject [52]: the authors developed a normalized index based on the well-known MAPO [66] index:

$$MAPO_{norm} = \frac{MAPO - MAPO_{10}}{MAPO_{50} - MAPO_{10}} \quad (Eq. 10)$$

This index is defined with the purpose of overcoming the following issues:

- Dispersion of sensors sensitivity (Figures 5 and 6) would directly reflect on MAPO evaluation, requiring a high calibration effort;
- Prototypes sensitivity to knocking phenomena is one order of magnitude greater compared to reference sensors (Figures 11 and 12): this is probably related to the fact that piezoelectric washers are both sensitive to pressure waves propagating inside the chamber and head mechanical vibrations.
- Piezo-electric washers are more susceptible to mechanical noise compared to reference sensors (Figure 13).

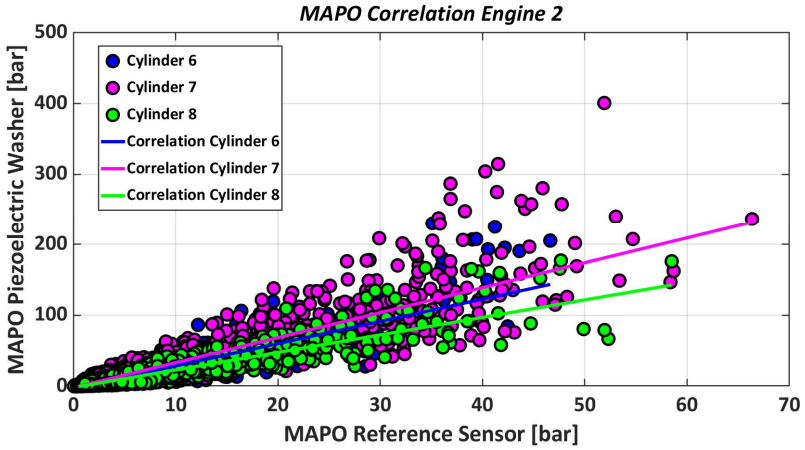


**Figure 11. Different correlations between the 3 piezoelectric washer sensors in comparison with the respective reference sensors. Data from engine 2, in operating points shown in Figure 10.**

The higher sensitivity to knock of the piezo-electric washer was already observed in [52], where a scale factor was applied to the threshold value used for the 99$^{th}$ percentile of the MAPO distribution, in order to compare the relative knock intensity assessed using the two sensors. The same approach could not be applied here, as different scale factors need to be applied to different cylinders. This behaviour can be clearly observed in Figure 11: the correlation lines that bind the MAPO indices evaluated with the washer (from now on referred to as Maximum Amplitude of Washer Oscillation MAWO) (y-axis) to the MAPO evaluated with reference sensor (x-axis) change from cylinder to cylinder.

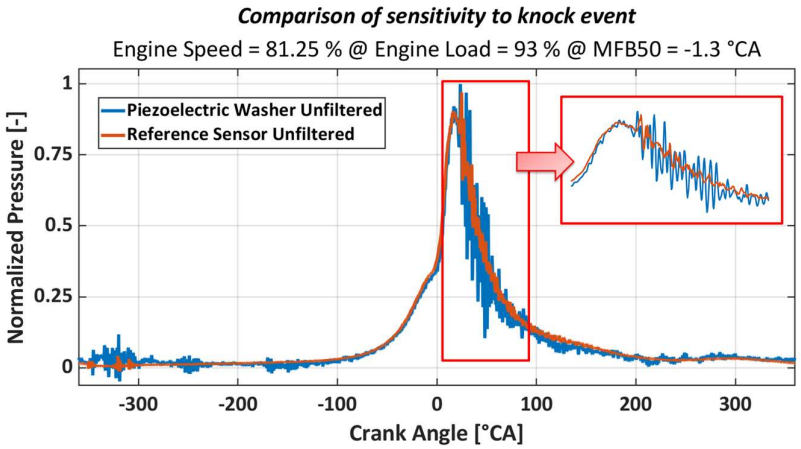


**Figure 12. Greater sensitivity to the knocking phenomena of piezo-electric washer compared to the reference sensor. Data from cylinder 6 engine 2.**

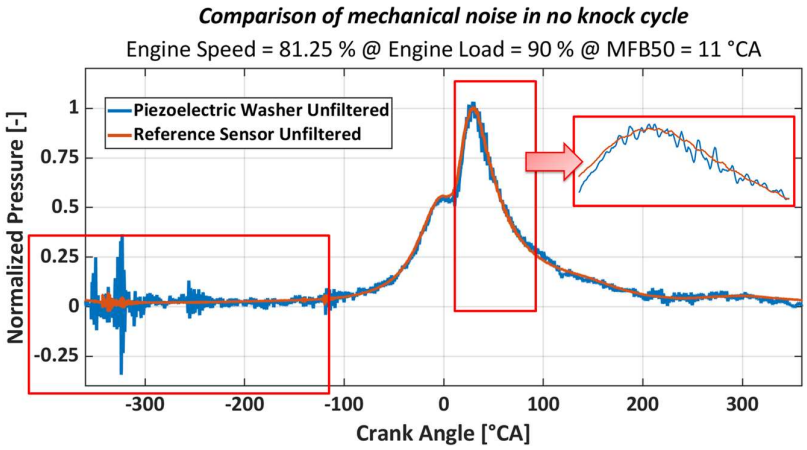


**Figure 13. No knock engine condition. Piezo-electric washer was more susceptible to mechanical noise compared to the reference sensor. Data from cylinder 6 engine 2.**

This dispersion in knock sensitivity can be attributed to a combination of several factors. First of all, sensitivity variations caused by the manufacturing process of prototypes, already discussed in Section 3, cause different sensitivities to pressure oscillations. Secondly, reference sensors are not positioned in the same spot as washer sensors inside the combustion chamber. As it is well known, the position of the pressure sensor within the combustion chamber greatly impacts the estimation of knock indexes [67, 68, 69]. Finally, as already remarked, MAWO intensity is also influenced by mechanical vibrations sensed by the washer, whose intensity may vary from cylinder to cylinder.

The normalized index in Eq. 10 makes it possible to overcome these issues. Using such normalization both on MAPO and MAWO, a comparable evaluation of knock intensity can be achieved with the washer and the reference sensor. As shown in Figure 14, percentile curves evaluated for reference and prototype sensors have similar shapes, although different scales. At low percentile values (<50%), however, the effect of mechanical noise has a high impact on MAWO, yielding a bias that cannot be observed on MAPO. Nevertheless, plots on the lower part of Figure 14 show that normalized traces of MAPO and MAWO are almost superimposed.

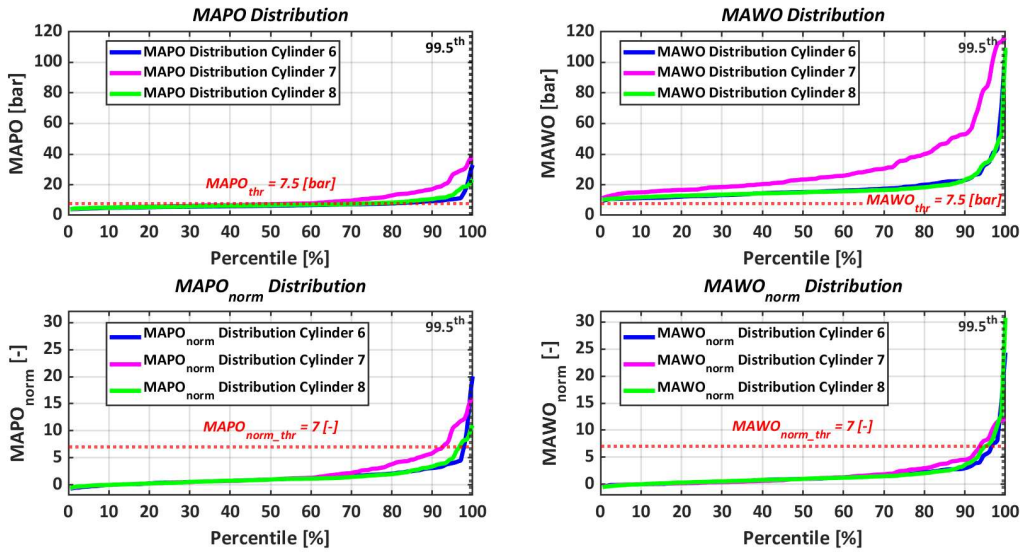


**Figure 14. Example of percentile curve for both reference and prototype sensor in knock condition on engine 2. (Engine Speed = 93.75 % @ Engine Load = 87 % @ MFB50 = -1.8 °CA).**

This approach offers an additional advantage: thanks to normalization, not only is it possible to make MAPO and MAWO indices comparable, but indices referring to different cylinders are automatically scaled.

Thresholds for the normalized indices (MAPO or MAWO) are defined based on data referring to knocking cycles of all instrumented cylinders. Each operating point is arbitrarily considered as knocking when 99.5$^{th}$ percentile exceeds a threshold defined using the following equation [70]:

$$MAPO_{thr} = \frac{Engine\ Speed\ (rpm)}{1000} \quad (Eq.11)$$

Comparing this absolute index with both $MAPO_{norm}$ and $MAWO_{norm}$ evaluated using Eq.3 at the same percentile, it was possible to find the normalized threshold ensuring correct knock detections. Table 5 summarizes the threshold levels referring to reference (MAPO) and normalized indices.

**Table 5. Summary of the tested working points and relative thresholds (absolute and normalized) found for the detection of the knock.**

| Engine Speed tested | $MAPO_{thr}$ (99.5$^{th}$) | $MAPO_{norm\ thr}$ (99.5$^{th}$) | $MAWO_{norm\ thr}$ (99.5$^{th}$) |
|---|---|---|---|
| 3500 rpm | 3.5 bar | 7 | 7 |
| 5500 rpm | 5.5 bar | 7 | 7 |
| 6500 rpm | 6.5 bar | 7 | 7 |
| 7500 rpm | 7.5 bar | 7 | 7 |

A valuable result obtained with this approach is that a unique threshold value, independent of sensor, cylinder, and also the operating condition (speed, load), is determined. In fact the threshold level used to assess knock intensity acceptance for the washer normalized index ($MAWO_{norm}$) and reference sensors normalized index ($MAPO_{norm}$) is the same (equal to 7), for all the cylinders and it does not change with engine speed.

Moreover, thanks to normalization all knock index distributions come closer (Figure 14). This is due to the fact that normalization aims at catching the shape of knock indices distribution, which does not depend on indices absolute value. The main drawback of this method is that it is capable of detecting knocking phenomena only in incipient or light-knock conditions, while in heavy knocking conditions it tends to

underestimate the percentage of knocking cycles [71]. The definition of $MAPO_{norm}$ and $MAWO_{norm}$ greatly depends on data samples of the considered distribution: the normalization factor defining the denominator of Equation 10 depends on the median of knock indices distribution. A high level of normalized index is only reached if current intensity is significantly higher than median. In a running condition where most of the engine cycles are knocking, this may lead to underestimate knock intensity, although mega-knock phenomena would still be captured. However, a knock controller usually starts decreasing the spark advance sooner than the previously described condition is reached.

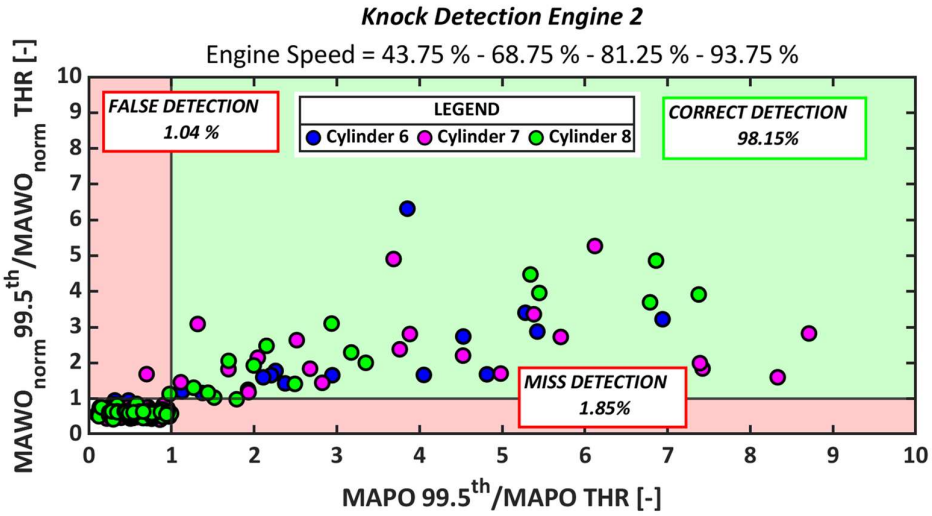


**Figure 15. Comparison of knock detection with reference sensor vs normalized approach using washer sensors. knock intensity indices are divided by the corresponding threshold value.**

Figure 15 presents data referring to four different engine speed conditions, where both knocking and non-knocking conditions were tested via spark advance sweeps. Each point in the graph represents a different running condition (i.e., different speed or spark advance setting). The ratio of normalized indices with the corresponding knock threshold (Table 5) is reported for MAPO on the x-axis and $MAWO_{norm}$ on the y-axis. It is easy to identify the tests where knock is correctly diagnosed or false positives and false negatives arise: the three prototype sensors clearly show good knock detection capabilities.

## 6. $P_{max}$ Estimation

As for MAPO analysis, also $P_{max}$ estimation is carried out based on the dataset from engine 2, since Electronic Control Unit (ECU) information useful to process washers data could only be accessed with the experimental setup used for engine 2.

The evaluation of $P_{max}$ cannot be completed with the piezo-electric signal only, due to the large sensitivity variations (Figure 3 and 4), which would lead to unacceptable inaccuracies. The correct sensitivity has to be estimated cycle-by-cycle, for example by using the pressure trace during compression stroke: the hypothesis of polytropic compression, provided that intake manifold pressure could be measured by other means, would allow to estimate the sensor sensitivity for any given engine cycle. However, this approach would require sample-by-sample processing of the signal, which is not necessarily possible in every combustion analyser (especially when integrated in the ECU).

As an alternative, peak pressure can be estimated with good accuracy [72] using a black box model whose inputs are:

- $MFB_{10}$
- $MFB_{50}$

- Initial Combustion Duration
- engine load index (relative load, rl)

initial combustion duration is evaluated as:

$$Initial\ Combustion\ Duration = \frac{MFB_{50} - MFB_{10}}{(RPM * \frac{6}{1000})} \quad (Eq. 12)$$

This black box model was developed using MATLAB. It is composed of a static Artificial Neural Network (ANN) with just one layer with 10 neurons. The neural network was trained with experimental data in order to build a response model that answered the following equation:

$$\frac{Firing\ P_{MAX}}{rl} = f(MFB_{10}, MFB_{50}, Initial\ Combustion\ Duration) \quad (Eq. 13)$$

In this way, engine firing peak pressure can be evaluated as:

$$Firing\ P_{MAX} = rl * f(MFB_{10}, MFB_{50}, Initial\ Combustion\ Duration) \quad (Eq. 14)$$

Rationale of such formulation is as follows: peak pressure depends on pressure during compression stroke, and on energy release. For SI engines, the latter can be roughly described by means of a triangular ROHR curve. While $MFB_{10}$ can be used to set the starting position of the ROHR trace, $MFB_{50}$ defines the position of ROHR peak. To determine the amplitude (the height of the triangle), information regarding the amount of energy that can be released is needed: in SI homogeneous stoichiometric combustions, this information can be retrieved from the amount of air filling the cylinder, i.e., rl. The same index also relates to the pressure reached during compression stroke. Finally, initial combustion duration indirectly adds the influence of engine speed to the process. In other words, a model using $MFB_{10}$, $MFB_{50}$, initial combustion duration, and RL as inputs should be able to output reliable values of maximum pressure.

Obviously, in a potential on-board application, $MFB_{10}$ and $MFB_{50}$ would be evaluated from the washer signal, while RL would be received by the ECU.

For the three instrumented cylinders, weights and bias of the model (Eq. 13) were defined using combustion indices ($MFB_{10}$, $MFB_{50}$, and $P_{max}$) evaluated from the reference signal with the objective of identifying the relationship between desired inputs and outputs, using the neural network. Once the proper parameters were found, the neural network was then tested using the inputs ($MFB_{10}$, $MFB_{50}$ and initial combustion duration) evaluated from the piezo-electric washers.

With the aim of developing a robust model without overfitting on training data, the neural network was tuned only on a portion of all available data. Then, the defined neural network was tested on the remaining portion of the dataset, hence verifying its predictability in no-training scenarios. Figure 16 presents data used to configure the parameters of the network (orange dots) and data used to verify the ANN predictability in no-training scenarios (green dots): as it can be noticed, only data sampled at 18.75 %, 43.75 %, 62.5 % and 93.75 % of maximum engine speed were used to train the model. Similarly, only a subset of available engine load setpoints were used.

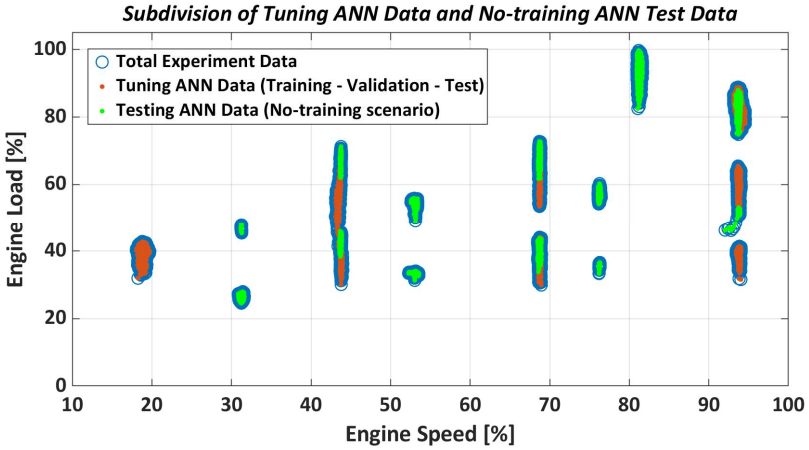


Figure 16. ANN tuning data and ANN testing data. Data from engine 2.

Table 6. Neural Network description.

| | |
|---|---|
| **Tuning Neural Network Data** | Training: 70% randomly selected data from orange dots in Figure 16<br>Validation: 15% randomly selected from orange dots in Figure 16<br>Test: 15% randomly selected data from orange dots in Figure 16 |
| **Number of hidden layers** | 1 |
| **Number of neurons** | 10 |
| **Network type** | Feed-forward back propagation |
| **Training function** | trainlm |
| **Adaption learning function** | learngdm |
| **Transfer function** | tansig |
| **Performance function** | Mean square error |
| **Stopping criteria** | Break the training of network when the validation mean square error grows for 26 consecutive iterations |

Figure 17 compares normalized $P_{max}$ values: data obtained using the reference sensor are reported on the x axis, while the y axis displays the output of the ANN model fed with information ($MFB_{10}$, $MFB_{50}$) gained from the reference sensor. The good reconstruction testifies model accuracy. Both the measured and the estimated pressure peak are normalized with respect to the maximum allowable pressure.

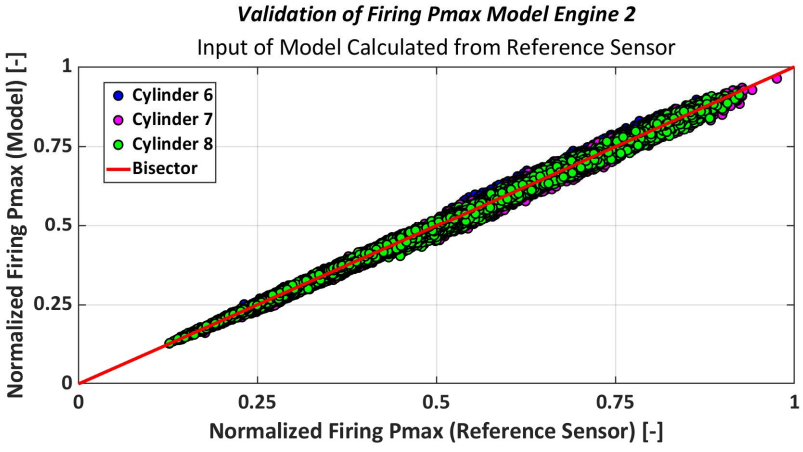


Figure 17. Normalized measured peak pressure vs normalized estimated peak pressure (ANN inputs evaluated from reference sensor).

Table 6 displays the synthetic correlation indices (RMSE and $R^2$) between black box model and reference sensor in assessing firing $P_{max.}$

**Table 7. Correlation indices on Firing Pmax estimation: Pmax model fed with reference sensor data on all operating points. Overall correlation with all three instrumented cylinders**

| Firing $P_{max}$ Model Input from Reference Sensor | | |
|---|---|---|
| **Instrumented Cylinder** | **RMSE [bar]** | **$R^2$[-]** |
| **Cylinder 6** | **1.76 [bar]** | **0.9979 [-]** |
| **Cylinder 7** | **1.76 [bar]** | **0.9982 [-]** |
| **Cylinder 8** | **1.48 [bar]** | **0.9987 [-]** |

Once the model is identified for the three cylinders, it is applied using as inputs combustion metrics ($MFB_{10}$, $MFB_{50}$, and Initial Combustion Duration) evaluated by means of the piezo-electric washer. Figure 18 displays the same results of Figure 17, with the only difference that values reported on the y axis are now obtained by feeding the ANN model with combustion metrics estimated by the washer.

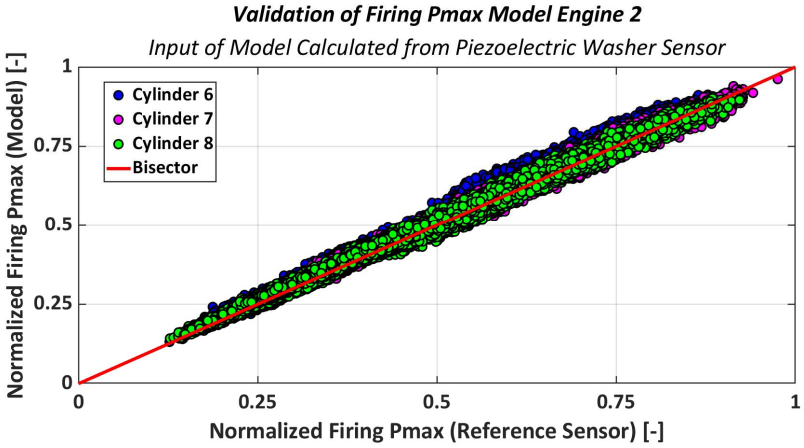


**Figure 18. Normalized measured peak pressure vs normalized estimated peak pressure (ANN inputs evaluated from washer sensor).**

Table 7 summarizes the correlation results (RMSE and $R^2$) displayed in Figure 18, achieved when prototype sensor data feeds the ANN $P_{max}$ mode.

**Table 7. Correlation indices on Firing Pmax estimation: Pmax model fed with piezo-electric washer sensor data on all operating points. Overall correlation with all three instrumented cylinders**

| Firing $P_{max}$ Model Input from Piezoelectric Washer Sensor | | |
|---|---|---|
| **Instrumented Cylinder** | **RMSE [bar]** | **$R^2$[-]** |
| **Cylinder 6** | **3.80 [bar]** | **0.9947 [-]** |
| **Cylinder 7** | **2.26 [bar]** | **0.9969 [-]** |
| **Cylinder 8** | **2.21 [bar]** | **0.9971 [-]** |

The Firing $P_{max}$ estimation based on the piezo-electric washer metrics is worse than that obtained with reference sensors. RMSE values (Table 7) are nearly twice as much compared to those obtained with reference sensors (Table 6): this is the result of model inaccuracies, in addition to those related to the determination of $MFB_{10}$ and $MFB_{50}$.

Despite these additional errors, the authors believe that the proposed methodology for the estimation of peak firing pressure still leads to satisfying results, with an average error always lower than 4 bar. This means

that the prototype sensors can also be used for on-board peak pressure estimation. In fact $P_{max}$ can be used for the development of closed-loop controls for reliability purposes [73].

## 7. Conclusions and Future Developments

This paper shows the results in determining significant combustion metrics using low-cost washer piezoelectric transducers for indirect in-cylinder pressure measurement. Despite some issues with sensor-sensitivity variability, it is proven that successful evaluation of the following combustion indices is possible:

- $MFB_{10}$, $MFB_{50}$, Firing $AP_{max}$
- Normalized knock intensity
- $P_{max}$, using ANN model

The comparison with metrics evaluated using reference lab sensors suggests that piezoelectric washers can be used for on-board combustion feedback control applications. Not only is the accuracy satisfying, but also the required economic effort seems to be compatible with on-board applications. In fact, the estimated cost of the piezo-electric washer in mass production is 10 to 100 times lower than the reference sensor, depending on production volumes.

However, prototypes washer sensors still present some unresolved issues that need to be corrected in order to further enhance sensors performance. Future studies will address:

- Thermal effects on sensor sensitivity (Figures 5 and 6)
- Pressure mis-estimation during expansion stroke (Figure 4).

Refinements in these areas should allow for better estimation of $MFB_{10}$, $MFB_{50}$, and Firing $AP_{max}$, while $P_{max}$ estimation should be significantly improved. In addition to this, a fairly accurate evaluation of other combustion metrics, such as $CHR_{max}$ and $IMEP_H$, would be possible. Future works will also allow to evaluate the use of piezoelectric washers as real time feedback for closed loop control systems on virtual engines.

## Symbols and Abbreviations

**$AP_{max}$** Crank angle at which the maximum value of the cylinder pressure is reached

**ATDC** Crank angle after cylinder top dead center

**ANN** Artificial Neural Network

**BTDC** Crank angle before cylinder top dead center

**°CA** Crank angle degrees

**CHR** Cumulate Heat Release

**$CHR_{max}$** Maximum value of the cumulate heat release

**$CO_2$** Carbon dioxide

**$E_b$** Young's modulus of the bolt

**ECU** Electronic Control Unit

**$E_j$** Young's modulus of the joint

**EOC** End Of Combustion

**Firing $AP_{max}$** Crank angle at which the maximum value of the cylinder pressure is reached during the combustion process

**Firing $P_{max}$** Maximum value of pressure assumed by the pressure inside the cylinder during the combustion process

**$F_p$** Force due to preload both on bolt and joint

**$F_x$** Additional force, function of bolt and joint force variation

**$F_j$** Force on the joint

**GDI** Gasoline Direct Injection

**GDCI** Gasoline Direct Compression Ignition

**GHG** Greenhouse Gasses

**ICE** Internal Combustion Engine

**IMEP** Indicating Mean Effective Pressure

**$IMEP_H$** Indicating Mean Effective Pressure evaluated on the indicated cycle with the intake and exhaust valves are closed

**MAP** Manifold Air Pressure

**MAPO** Maximum Absolute Pressure Oscillation

**$MAPO_{10}$** Tenth percentile value of the MAPO index

**$MAPO_{50}$** Fiftieth percentile value of the MAPO index

**$MAPO_{norm}$** Normalized knock index evaluated on the reference sensor signal

**$MAPO_{thr}$** Threshold value of the MAPO index used for the detection of the knocking phenomena

**MAWO** Maximum absolute pressure oscillation evaluated on the prototype signal

**$MAWO_{norm}$** Normalized knock index evaluated on the prototype sensor signal

**$MFB_{10}$** Crank angle at which the 10% of fuel mass inside the cylinder is burnt

**$MFB_{50}$** Crank angle at which the 50% of fuel mass inside the cylinder is burnt

**$MFB_{90}$** Crank angle at which the 90% of fuel mass inside the cylinder is burnt

**OEM** Original Equipment Manufacturer

**P** Pressure inside the combustion chamber

**PCB** Printed Circuit Boards

**PFI** Port Fuel Injection

**$P_{max}$** Maximum value assumed by the pressure inside the combustion chamber

**$R^2$** Bravais-Pearson correlation coefficient

**RCCI** Reactivity Controlled Compression Ignition

**RDE** Real Driving Emission

**RMSE** Root Mean Square Error

**ROHR** Rate Of Heat Release

**RPM** Revolutions Per Minute

**SACI** Spark Assisted Compression Ignition

**SOC** Start Of Combustion

**TJI** Turbulent Jet Ignition

**V** Volume inside the combustion chamber

**dP** Derivative of the pressure inside the combustion chamber

**dV** Derivative of the volume inside the combustion chamber

**dθ** Derivative angle

**k** Adiabatic index

**rl** relative load evaluated by the engine control unit

**$\Delta F_b$** Bolt force variation

**$\Delta F_c$** Joint force variation

**$\Delta L_b$** Bolt deformation

**$\Delta t_j$** Joint deformation

**Δδ** Bolt and joint strain variation

**θ** Crank Angle

**$\theta_{start}$** Starting crank angle of the angular window for the evaluation of CHR

$\theta_{end}$ Final crank angle of the angular window for the evaluation of CHR

## Appendix

This section shows the technical characteristics of the reference sensors and piezo-electric washer used for each engine.

**Table 8. Technical data of reference sensor used on engines 1 - 3.**

| M12x1.25 measuring spark plug with integrated 3 mm cylinder pressure sensor Type 6115C | | |
|---|---|---|
| Manufacturer | Kistler | |
| Measuring range | bar | 0 … 200 |
| Overload | bar | 250 |
| Sensitivity at 200 °C | pC/bar | ≈-10 |
| Sensor operating temperature range | °C | -20 … 350 |
| Thermal sensitivity shift<br>200 ± 50 °C | % | <±1 |

**Table 9. Technical data of reference sensor used on engine 2.**

| Water - cooled pressure sensor for combustion engines Type 6061C | | |
|---|---|---|
| Manufacturer | Kistler | |
| Measuring range | bar | 0 … 250 |
| Overload | bar | 300 |
| Sensitivity at 200°C | pC/bar | ≈-26 |
| Sensor operating temperature range (uncooled) | °C | -40 … 350 |
| Thermal sensitivity shift<br>RT … 350 °C (uncooled)<br>50 °C … ± 30 °C (cooled) | <br>%<br>% | <br>±3<br>±0.2 |

**Table 10. Technical data of piezo-electric washer sensor used on engines 1 - 2 - 3**

| M12 - M10 piezo-electric washer | | |
|---|---|---|
| Sensor thickness | mm | 1.9 … 2 |
| Measuring range | bar | 0 … >300 |
| Overload | bar | NA |
| Sensitivity at 100°C | pC/bar | 70 … 120 |
| Sensor operating temperature range | °C | <175 |
| Thermal sensitivity shift<br>-20 °C … 125 °C | <br>% | <br>0…4 |

## Literature


[1] Johnson, T., "**Diesel Emission Control in Review,**" SAE Int. J. Fuels Lubr. 1(1):68-81, 2009, https://doi.org/10.4271/2008-01-0069.

[2] Johnson, T. and Joshi, A., "**Review of Vehicle Engine Efficiency and Emissions,**" SAE Technical Paper 2017-01-0907, 2017, https://doi.org/10.4271/2017-01-0907.

[3] Dadam, S., Nieuwstadt, M., Lehmen, A., Ravi, V., Kumar, V., Bhat, R., "**A Unique Application of Gasoline Particulate Filter Pressure Sensing Diagnostics,**" SAE International Journal of Passenger Cars - Mechanical Systems, 2021-08-06, 2021, https://doi.org/10.4271/06-14-02-0007.

[4] Roberts, P.J., Mumby, R., Mason, A., Redford-Knight, L. et al., "**RDE Plus - The Development of a Road, Rig and Engine-in-the-Loop Test Methodology for Real Driving Emissions Compliance,**" SAE Technical Paper 2019-01-0756, 2019, https://doi.org/10.4271/2019-01-0756.

[5] Mock P., "**CO2 Emission Standards for Passenger Cars and Light-Commercial Vehicles in the European Union**," https://theicct.org/sites/default/files/publications/EU-LCV-CO2-2030_ICCTupdate_20190123.pdf, 2019, accessed 09.01.2019.

[6] Dadam, S., Imtiaz, A., Di, Z., Vivek, K., "**Effects of Differential Pressure Measurement Characteristics on High Pressure-EGR Estimation Error in SI-Engines.**" International Journal of Engine Research, (November 2021). https://doi.org/10.1177/14680874211055580.

[7] Katic, Vladimir & Dumnic, Boris & Corba, Zoltan & Milicevic, Dragan. (2014). **Electrification of The Vehicle Propulsion System – An Overview**. Facta Universitatis - series: Electronics and Energetics. 27. 299-316. http://dx.doi.org/10.2298/FUEE1402299K.

[8] Albrahim, M., Zahrani, A.A., Arora, A. *et al.* **An overview of key evolutions in the light-duty vehicle sector and their impact on oil demand**. *Energy Transit* **3,** 81–103 (2019). https://doi.org/10.1007/s41825-019-00017-7

[9] O.V. Marchenko, S.V. Solomin, **The future energy: Hydrogen versus electricity**, International Journal of Hydrogen Energy, Volume 40, Issue 10, 2015, Pages 3801-3805, ISSN 0360-3199, https://doi.org/10.1016/j.ijhydene.2015.01.132

[10] L. Liu, S. Y. Cheng, J. B. Li & Y. F. Huang (2007) **Mitigating Environmental Pollution and Impacts from Fossil Fuels: The Role of Alternative Fuels**, Energy Sources, Part A: Recovery, Utilization, and Environmental Effects, 29:12, 1069-1080, DOI: 10.1080/15567030601003627

[11] L. Situ, "**Electric Vehicle development: The past, present & future,**" *2009 3rd International Conference on Power Electronics Systems and Applications (PESA)*, 2009, pp. 1-3.

[12] Zhang, Runsen & Fujimori, Shinichiro. (2019). **The role of transport electrification in global climate change mitigation scenarios**. Environmental Research Letters. 15. https://iopscience.iop.org/article/10.1088/1748-9326/ab6658.

[13] Alexander Wanitschke, Simon Hoffmann, **Are battery electric vehicles the future? An uncertainty comparison with Hydrogen and combustion engines**, Environmental Innovation and Societal Transitions, Volume 35, 2020, Pages 509-523, ISSN 2210-4224, https://doi.org/10.1016/j.eist.2019.03.003.

[14] Eckhard Karden, Servé Ploumen, Birger Fricke, Ted Miller, Kent Snyder, **Energy storage devices for future hybrid electric vehicles**, Journal of Power Sources, Volume 168, Issue 1, 2007, Pages 2-11, ISSN 0378-7753, https://doi.org/10.1016/j.jpowsour.2006.10.090.

[15] Macioszek E. (2020) **Electric Vehicles - Problems and Issues**. In: Sierpiński G. (eds) Smart and Green Solutions for Transport Systems. TSTP 2019. Advances in Intelligent Systems and Computing, vol 1091. Springer, Cham. https://doi.org/10.1007/978-3-030-35543-2_14.

[16] Dadam, S., Jentz, R., lenzen, T., and Meissner, H., "**Diagnostic Evaluation of Exhaust Gas Recirculation (EGR) System on Gasoline Electric Hybrid Vehicle,**" SAE Technical Paper 2020-01-0902, 2020, https://doi.org/10.4271/2020-01-0902

[17] Chung I., Kang H., Park J., Lee J. **"Fuel economy improvement analysis of hybrid electric vehicle"**. International Journal of Automotive Technology, Vol. 20, No. 3, pp. 531−537 (2019), https://doi.org/10.1007/s12239-019-0050-7.

[18] Solouk, A., Shakiba-herfeh, M., Kannan, K., Solmaz, H. et al., **"Fuel Economy Benefits of Integrating a Multi-Mode Low Temperature Combustion (LTC) Engine in a Series Extended Range Electric Powertrain,"** SAE Technical Paper 2016-01-2361, 2016, https://doi.org/10.4271/2016-01-2361.

[19] Takahashi, D., Nakata, K., Yoshihara, Y., Ohta, Y. et al., **"Combustion Development to Achieve Engine Thermal Efficiency of 40% for Hybrid Vehicles,"** SAE Technical Paper 2015-01-1254, 2015, https://doi.org/10.4271/2015-01-1254.

[20] S. Overington and S. Rajakaruna, "**High-Efficiency Control of Internal Combustion Engines in Blended Charge Depletion/Charge Sustenance Strategies for Plug-In Hybrid Electric Vehicles,**" in *IEEE Transactions on Vehicular Technology*, vol. 64, no. 1, pp. 48-61, Jan. 2015, https://doi.org/10.1109/TVT.2014.2321454.

[21] Ciampolini M., Ferrara G., **"Low Temperature Combustion The future of Internal Combustion Engines,"** https://e-l.unifi.it/pluginfile.php/615503/mod_resource/content/1/SI-LTC.pdf, 2019.

[22] Krishnamoorthi M., Malayalamurthi R., He Z., Kandasamy S., **"A review on low temperature combustion engines: Performance, combustion and emission characteristics",** Renewable and Sustainable Energy Reviews 2019; https://doi.org/10.1016/j.rser.2019.109404.

[23] M, M. and Krishnasamy, A., "**A Comparison of Different Low Temperature Combustion Strategies in a Small Single Cylinder Diesel Engine under Low Load Conditions,**" SAE Technical Paper 2017-01-2363, 2017, https://doi.org/10.4271/2017-01-2363.

[24] Cho, K., Latimer, E., Lorey, M., Cleary, D. et al., "**Gasoline Fuels Assessment for Delphi's Second Generation Gasoline Direct-Injection Compression Ignition (GDCI) Multi-Cylinder Engine,**" SAE Int. J. Engines 10(4):1430-1442, 2017, https://doi.org/10.4271/2017-01-0743.

[25] Sequino, L., Mancaruso, E., Monsalve-Serrano, J., and Garcia, A., "**Infrared/Visible Optical Diagnostics of RCCI Combustion with Dieseline in a Compression Ignition Engine,**" SAE Int. J. Adv. & Curr. Prac. in Mobility 2(3):1411-1421, 2020, https://doi.org/10.4271/2020-01-0557.

[26] Triantopoulos, V., Bohac, S., Martz, J., Lavoie, G. et al., "**The Effect of EGR Dilution on the Heat Release Rates in Boosted Spark-Assisted Compression Ignition (SACI) Engines,**" SAE Int. J. Adv. & Curr. Prac. in Mobility 2(4):2183-2195, 2020, https://doi.org/10.4271/2020-01-1134.

[27] Hua, J., Zhou, L., Gao, Q., Feng, Z. et al., "**Effects on Cycle-to-Cycle Variations and Knocking Combustion of Turbulent Jet Ignition (TJI) with a Small Volume Pre-Chamber,**" SAE Technical Paper 2020-01-1119, 2020, https://doi.org/10.4271/2020-01-1119.

[28] Alvarez CEC, Couto GE, Roso VR, Thiriet AB, Valle RM. **"A review of prechamber ignition systems as lean combustion technology for SI engines"**. Applied Thermal Engineering 2018; 128:107–20; https://doi.org/10.1016/j.applthermaleng.2017.08.118.

[29] Claudia Bassano, Paolo Deiana, Luca Lietti, Carlo Giorgio Visconti, **P2G movable modular plant operation on synthetic methane production from CO2 and Hydrogen from renewables sources**, Fuel, Volume 253, 2019, Pages 1071-1079, ISSN 0016-2361, https://doi.org/10.1016/j.fuel.2019.05.074.

[30] R. Luque, J.G. Speight, 1 - **Gasification and synthetic liquid fuel production: an overview**, Editor(s): Rafael Luque, James G. Speight, In Woodhead Publishing Series in Energy, Gasification for Synthetic Fuel Production, Woodhead Publishing, 2015, Pages 3-27, ISBN 9780857098023, https://doi.org/10.1016/B978-0-85709-802-3.00001-1.

[31] Alexander Buttler, Hartmut Spliethoff, **Current status of water electrolysis for energy storage, grid balancing and sector coupling via power-to-gas and power-to-liquids: A review, Renewable and**

**Sustainable Energy Reviews**, Volume 82, Part 3, 2018, Pages 2440-2454, ISSN 1364-0321, https://doi.org/10.1016/j.rser.2017.09.003.

[32] Olga Bičáková, Pavel Straka, **Production of Hydrogen from renewable resources and its effectiveness**, International Journal of Hydrogen Energy, Volume 37, Issue 16, 2012, Pages 11563-11578, ISSN 0360-3199, https://doi.org/10.1016/j.ijhydene.2012.05.047.

[33] Albrecht, M., Deeg, H., Schwarzenthal, D., and Eilts, P., **"The Influence of Fuel Composition and Renewable Fuel Components on the Emissions of a GDI Engine,"** SAE Technical Paper 2020-37-0025, 2020, https://doi.org/10.4271/2020-37-0025.

[34] Rossi, E., Hummel, S., Cupo, F., Vacca, A. et al., **"Experimental and Numerical Investigation for Improved Mixture Formation of an eFuel Compared to Standard Gasoline,"** SAE Technical Paper 2021-24-0019, 2021, https://doi.org/10.4271/2021-24-0019.

[35] Yip, Ho L., Aleš Srna, Anthony C.Y. Yuen, Sanghoon Kook, Robert A. Taylor, Guan H. Yeoh, Paul R. Medwell, and Qing N. Chan 2019. "**A Review of Hydrogen Direct Injection for Internal Combustion Engines: Towards Carbon-Free Combustion**" *Applied Sciences* 9, no. 22: 4842. https://doi.org/10.3390/app9224842.

[36] Nazim Z. Muradov, T. Nejat Veziroğlu, **"Green" path from fossil-based to Hydrogen economy: An overview of carbon-neutral technologies**, International Journal of Hydrogen Energy, Volume 33, Issue 23, 2008, Pages 6804-6839, ISSN 0360-3199, https://doi.org/10.1016/j.ijhydene.2008.08.054.

[37] Sopena, C. & Diéguez, P.M. & Sáinz, D. & Urroz, J.C. & Guelbenzu, Eugenio & Gandía, Luis M.. (2010). **Conversion of a commercial spark ignition engine to run on Hydrogen: Performance comparison using Hydrogen and gasoline**. International Journal of Hydrogen Energy. 35. 1420-1429. 10.1016/j.ijhydene.2009.11.090.

[38] Sebastian Verhelst, Thomas Wallner, **Hydrogen-fueled internal combustion engines, Progress in Energy and Combustion Science**, Volume 35, Issue 6, 2009, Pages 490-527, ISSN 0360-1285, https://doi.org/10.1016/j.pecs.2009.08.001.

[39] Nakai, E., Goto, T., Ezumi, K., Tsumura, Y., Endou, K., Kanda, Y., ... & Hitomi, M. (2019, October). **Mazda Skyactiv-X 2.0 L Gasoline Engine**. In 28th Aachen Colloquium Automobile and Engine Technology (pp. 55-78). Presented at 28th Aachen Colloquium Automobile and Engine Technology 2019.

[40] Hailin Li, Ghazi A. Karim, **Knock in spark ignition Hydrogen engines**, International Journal of Hydrogen Energy, Volume 29, Issue 8, 2004, Pages 859-865, ISSN 0360-3199, https://doi.org/10.1016/j.ijhydene.2003.09.013.

[41] S. Szwaja, K.R. Bhandary, J.D. Naber, **Comparisons of Hydrogen and gasoline combustion knock in a spark ignition engine**, International Journal of Hydrogen Energy, Volume 32, Issue 18, 2007, Pages 5076-5087, ISSN 0360-3199, https://doi.org/10.1016/j.ijhydene.2007.07.063.

[42] Ravaglioli, V., Carra, F., Moro, D., De Cesare, M. et al., "**Remote Sensing Methodology for the Closed-Loop Control of RCCI Dual Fuel Combustion,**" SAE Technical Paper 2018-01-0253, 2018, https://doi.org/10.4271/2018-01-0253.

[43] Carlucci A.P., Laforgia D., Motz S., Saracino R., Wenzel S.P. **"Advanced closed loop combustion control of a LTC diesel engine based on in-cylinder pressure signals".** Energy Conversion and Management 2014; 77:193–207, https://doi.org/10.1016/j.enconman.2013.08.054.

[44] De Cesare, M., Ravaglioli, V., Carra, F., and Stola, F., **"Review of Combustion Indexes Remote Sensing Applied to Different Combustion Types,"** SAE Technical Paper 2019-01-1132, 2019, https://doi.org/10.4271/2019-01-1132.

[45] Ponti, F., **"Indicated Torque Estimation Using a Torsional Behavior Model of the Engine,"** SAE Technical Paper 2005-01-3761, 2005, https://doi.org/10.4271/2005-01-3761.

[46] Cavina, N., Sgatti, S., Cavanna, F., and Bisanti, G., "**Combustion Monitoring Based on Engine Acoustic Emission Signal Processing,**" SAE Technical Paper 2009-01- 1024, 2009, https://doi.org/10.4271/2009-01-1024.

[47] Fiorini, N., Romani, L., Bellissima, A., Vichi, G., Bianchini, A., Ferrara, G., "**An indirect in-cylinder pressure measurement technique based on the estimation of the mechanical strength acting on an engine head screw: development and assessment**," Energy Procedia, Volume 148, 2018, Pages 695-702, ISSN 1876-6102, https://doi.org/10.1016/j.egypro.2018.08.159.

[48] Bernard R. Teitelbaum, John P. Carrico, **Integrated spark plug-combustion pressure sensor**. US Patent 4,169,388, Dec 13, 1978.

[49] Randall, K. and Powell, J., **"A Cylinder Pressure Sensor for Spark Advance Control and Knock Detection,"** SAE Technical Paper 790139, 1979, https://doi.org/10.4271/790139.

[50] Shimasaki, Y., Kobayashi, M., Sakamoto, H., Ueno, M. et al., "**Study on Engine Management System Using In-cylinder Pressure Sensor Integrated with Spark Plug,**" SAE Technical Paper 2004-01-0519, 2004, https://doi.org/10.4271/2004-01-0519.

[51] Fiorini, N., Romani, L., Ferrara, G., Vichi, G., Bellissima, A., Go, A., Ryota, M., "**A methodology for the estimation of in-cylinder pressure in a four-stroke internal combustion engine based on the combination of a strain washer signal with a 0D thermodynamic model**", AIP Conference Proceedings 2191, 020073 (2019) https://doi.org/10.1063/1.5138806.

[52] Corti, E., Abbondanza, M., Ponti, F., and Raggini, L., "**The Use of Piezoelectric Washers for Feedback Combustion Control,**" SAE Int. J. Adv. & Curr. Prac. in Mobility 2(4):2217-2228, 2020, https://doi.org/10.4271/2020-01-1146.

[53] Fukuoka, T., **Threaded Fasteners for Engineers and Design - Solid Mechanics and Numerical Analysis** (Corona Publishing Co Ltd, 2015).

[54] Joseph E.Shigley, Charles R. Mischke, **"Standard Handbook of Machine Design"**, McGrawHill 1996, second edition, pag. 727-729

[55] D. Zakarian, A. Khachatrian, S. Firstov, **Universal temperature dependence of Young's modulus**, Metal Powder Report,Volume 74, Issue 4,2019,Pages 204-206,ISSN 0026-0657, https://doi.org/10.1016/j.mprp.2018.12.079.

[56] P.P Singh, Munish Kumar, F**Temperature dependence of bulk modulus and second-order elastic constants**, Physica B: Condensed Matter, Volume 344, Issues 1–4, 2004, Pages 41-51, ISSN 0921-4526, https://doi.org/10.1016/j.physb.2003.07.012.

[57] G. Rajaram, S. Kumaran, T. Srinivasa Rao, **High temperature tensile and wear behaviour of aluminum silicon alloy**, Materials Science and Engineering: A, Volume 528, Issue 1, 2010, Pages 247-253, ISSN 0921-5093, https://doi.org/10.1016/j.msea.2010.09.020.

[58] J. Herrmann, G. Inden, G. Sauthoff, **Deformation behaviour of iron-rich iron-aluminium alloys at high temperatures**, Acta Materialia, Volume 51, Issue 11, 2003, Pages 3233-3242, ISSN 1359-6454, https://doi.org/10.1016/S1359-6454(03)00144-7.

[59] Maurya, R.K., **Characteristics and Control of Low- Temperature Combustion Engines**, Springer International Publishing, 2018, ISBN:978-3-319-68507-6, http://doi.org/10.1007/978-3-319-68508-3.

[60] Ravaglioli, V. and Bussi, C., "**Model-Based Pre-Ignition Diagnostics in a Race Car Application,**" Energies, MDPI, Open Access Journal 12(12):1-12, June 2019, https://doi.org/10.3390/en12122277.

[61] Heywood, J.B., **Internal Combustion Engine Fundamentals** (McGraw Hill Professionals, 2018), ISBN:1260116115.

[62] Shimasaki, Y., Kobayashi, M., Sakamoto, H., Ueno, M. et al., **Pressure Sensor Integrated with Spark Plug,**" SAE Technical Paper 2004-01-0519, 2004, https://doi.org/10.4271/2004-01-0519.

[63]. Sawamoto, K., Kawamura, Y., Kita, T., and Matsushita, K., "**Individual Cylinder Knock Control by Detecting Cylinder Pressure,**" SAE Technical Paper 871911, 1987, https://doi.org/10.4271/871911.

[64] Morris, J., "**Intra-Cylinder Combustion Pressure Sensing**," SAE Technical Paper 870816, 1987, https://doi.org/10.4271/870816.

[65] Corrigan, D. and Fontanesi, S., "**Knock: A Century of Research,**" SAE Int. J. Engines 15(1):2022, https://doi.org/10.4271/03-15-01-0004.

[66] Xudong Zhen, Yang Wang, Shuaiqing Xu, Yongsheng Zhu, Chengjun Tao, Tao Xu, Mingzhi Song, **"The engine knock analysis – An overview"**, Applied Energy, Volume 92, 2012, Pages 628-636, ISSN 0306-2619, https://doi.org/10.1016/j.apenergy.2011.11.079.

[67] Bengisu, T., "Computing The Optimum Knock Sensor Locations," SAE Technical Paper 2002-01-1187, 2002, https://doi.org/10.4271/2002-01-1187.

[68] Horner, T., "**Knock Detection Using Spectral Analysis Techniques on a Texas Instruments TMS320 DSP,**" SAE Technical Paper 960614, 1996, https://doi.org/10.4271/960614.

[69] Corrigan, D.J., Breda, S., and Fontanesi, S., "**A Simple CFD Model for Knocking Cylinder Pressure Data Interpretation: Part 1,**" SAE Technical Paper 2021-24-0051, 2021, https://doi.org/10.4271/2021-24-0051.

[70] Cavina, N., Rojo, N., Businaro, A., and Cevolani, R., "**Comparison between Pressure- and Ion-Current-Based Closed-Loop Combustion Control Performance,**" SAE Int. J. Engines 12(2):219-230, 2019, https://doi.org/10.4271/03-12-02-0016.

[71] Sandro Gail, Roger F. Cracknell, Dáire Corrigan, Andrea Festa, Varun Shankar, Benoit Poulet, Guy Lovett, Rene D. Büttgen, Karl A. Heufer, Roberto Mariconti, Matteo Cucchi, Fabio Mortellaro, **Evaluating a novel gasoline surrogate containing isopentane using a rapid compression machine and an engine**, Proceedings of the Combustion Institute, Volume 38, Issue 4, 2021, Pages 5643-5653, ISSN 1540-7489, https://doi.org/10.1016/j.proci.2020.07.103.

[72] Scocozza, G., Silvagni, G., Brusa, A., Cavina, N. et al., "**Development and Validation of a Virtual Sensor for Estimating the Maximum in-Cylinder Pressure of SI and GCI Engines**," SAE Technical Paper 2021-24-0026, 2021, https://doi-org.ezproxy.unibo.it/10.4271/2021-24-0026.

[73] Brusa, A.; Cavina, N.; Rojo, N.; Mecagni, J.; Corti, E.; Ravaglioli, V.; Cucchi, M.; Silvestri, N. "**Development and Experimental Validation of an Adaptive, Piston-Damage-Based Combustion Control System for SI Engines: Part 1—Evaluating Open-Loop Chain Performance."** Energies 2021, 14, 5367. https://doi.org/10.3390/en14175367.